RSC Advances

PAPER

View Article Online
View Journal | View Issue



Cite this: *RSC Adv.*, 2026, **16**, 28768

# Synergistic dual-interface modification for high-performance $CsPbBr_3$ perovskite solar cells: a combined experimental and modeling study

Xinghua Li,[ab] Zhongchen Bai,[*c] Qixin Chen[ad] and Zhengping Zhang*[a]

All-inorganic $CsPbBr_3$ perovskite solar cells (PSCs) suffer from efficiency losses due to their interfacial energy level mismatch. Herein, we propose a synergistic dual-interface modification strategy to improve the photoelectrical performance of C/$CsPbBr_3$/$SnO_2$-structure PSCs. At the $CsPbBr_3$/carbon interface, *N*,*N*′-dicyclohexylcarbodiimide (DCC) could elevate the $CsPbBr_3$ Fermi level to suppress the interfacial non-radiative recombination to increase the open-circuit voltage ($V_{OC}$). At the $SnO_2$/$CsPbBr_3$ interface, $NH_4F$ could upshift the $SnO_2$ Fermi level to enhance the crystallinity of $CsPbBr_3$ to markedly improve the fill factor (FF). The optimized device could achieve a power conversion efficiency of 9.59% with a $V_{OC}$ of 1.53 V and an FF of 82.4%. To elucidate the underlying mechanism, we established a dual-diode series model (DDSM), which revealed that the $V_{OC}$ was governed by the $CsPbBr_3$/carbon barrier and the FF was controlled by the $SnO_2$/$CsPbBr_3$ barrier. The theoretical predictions were consistent with the experimental results, providing a robust framework for designing high-performance all-inorganic PSCs.

Received 8th April 2026
Accepted 13th May 2026

DOI: 10.1039/d6ra02943d

rsc.li/rsc-advances



## 1. Introduction

The all-inorganic perovskite $CsPbBr_3$ has attracted considerable attention for photovoltaic applications owing to its wide bandgap (~2.3 eV), excellent thermal stability, and oxidation resistance.[1–3] Conventional $CsPbBr_3$ perovskite solar cells (PSCs) consist of an electron transport layer (ETL), a $CsPbBr_3$ light-absorbing layer, a hole transport layer (HTL) and a carbon electrode (Fig. 1).

However, compared with $MAPbI_3$-based devices, $CsPbBr_3$-based devices suffer from significantly higher $V_{OC}$ losses of up to 0.6 V, which severely limits their efficiency.[4] Early studies attributed this loss to halogen phase separation.[5] However, subsequent work has shown that the loss persists even without pronounced phase separation and is primarily caused by deep-level defects that induce non-radiative recombination.[6] Therefore, defect passivation is a key strategy for improving device performance. Some significant progress has been achieved through crystallization control,[7–9] additive engineering,[10–12] and interface modification.[13–15] Notably, a recent study by Shahriar *et al.* demonstrated that LiTFSI treatment could effectively passivate interfacial defects by reducing oxygen vacancies. It could also optimize the energy level alignment between the perovskite active layer and the ETL, thereby enhancing both the conductivity and the efficiency of charge carrier extraction.[16]

In addition to defect-induced recombination, the energy level mismatch between $CsPbBr_3$ and its adjacent charge transport layers also significantly contributes to $V_{OC}$ loss. Various energy level modulation strategies have been developed, including interface modification at the $CsPbBr_3$/carbon contact[17–19] and doping strategies for adjusting Fermi levels.[20,21] However, these strategies typically focus on a single interface due to the lack of a systematic understanding of how to decouple the contributions of each interface to the $V_{OC}$ and fill factor (FF).

FF is another critical parameter affecting device performance. In wide-bandgap perovskite cells with a well-passivated interface, FF is primarily limited by carrier recombination.[22] Further investigations have revealed that FF loss is strongly correlated with interfacial recombination, particularly at the perovskite/hole transport layer interface,[23] where hole extraction is the rate-limiting step. Consequently, some studies have

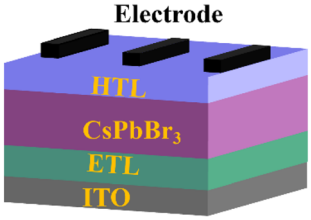


Fig. 1 Diagram of the structure of a $CsPbBr_3$ solar cell.

[a]*College of Big Data and Information Engineering, Guizhou University, Guiyang City, 550025, China. E-mail: zpzhang@gzu.edu.cn*

[b]*College of Electronics and Information Engineering, Anshun University, Anshun City, 561000, China*

[c]*College of Medicine, Guizhou University, Guiyang City, 550025, China. E-mail: zcbai@gzu.edu.cn*

[d]*Guizhou Polytechnic of Construction, Guiyang City, 551499, China*

employed dual hole transport layers to enhance hole mobility[24] or optimized energy level alignment to improve hole extraction efficiency.[25] Rong-Ho Lee *et al.* introduced CPAM as an interfacial modification layer at the $NiO_x$/$MAPbI_3$ interface to improve both the interfacial contact and the energy level alignment. Compared with pristine samples, the PVSCs fabricated with a CPAM-modified $NiO_x$ layer had significantly enhanced performance.[26] Currently, research on carbon-based $CsPbBr_3$ solar cells is mainly focused on suppressing non-radiative recombination through interface and doping engineering. However, the precise mechanism by which interfacial contact can govern distinct photovoltaic parameters, and specifically, the decoupling of the effects on open-circuit voltage and fill factor, remains unclear. This ambiguity hinders the rational design of high-performance devices.

In this study, we propose a synergistic interfacial modification strategy based on the introduction of *N*,*N*′-dicyclohexylcarbodiimide (DCC) at the $CsPbBr_3$/carbon interface and $NH_4F$ at the $SnO_2$/$CsPbBr_3$ interface to improve the photoelectrical performance of $CsPbBr_3$ PSCs. To fundamentally understand how these interfaces dictate device performance, we innovatively established a dual-diode series model (DDSM) based on carrier transport theory. By deriving the current–voltage (*J*–*V*) characteristic equations, we quantitatively elucidated the relationship between key performance metrics and their corresponding interfacial barriers, providing a theoretical foundation for optimizing energy level alignment in all-inorganic PSCs.

## 2. Results and discussion

Details regarding the device fabrication and characterization methods are provided in Note S2.

### 2.1 Influence of DCC at the $CsPbBr_3$/carbon interface

As shown in Fig. 2(a and b), the cutoff energy and onset binding energy of $CsPbBr_3$ are shifted after interfacial modification with DCC. The Fermi level of $CsPbBr_3$ increases by approximately 0.18 eV, which is attributed to an interfacial dipole effect between $CsPbBr_3$ and the DCC molecules.[27] The origin of these dipoles can be explained by the interaction of $CsPbBr_3$ with the DCC molecules, which is shown in Fig. 2(c). Moreover, a charge density difference is induced by DCC molecules adsorbed on the $CsPbBr_3$ surface. The model was constructed on the basis of monodentate coordination, as the adjacent Pb atoms are separated by 8.244 Å and 5.868 Å along the crystallographic *a*- and *b*-axes, respectively (Fig. S2(a)), rendering bridging coordination unfeasible. Accordingly, a monodentate coordination model was adopted (Fig. S2(b)); the DFT calculation parameters are provided in Fig. S3 and S4. The charge density difference map in Fig. 2(c) reveals electron transfer from the vicinity of the nitrogen atoms toward the Pb dangling bonds (indicated by purple arrows), confirming the formation of coordination bonds. Concomitant with this charge transfer, a dipole pointing from the DCC molecule toward the $CsPbBr_3$ interface is established.

Fig. 2(d) shows that after DCC modification, the PL peak intensity increases significantly, indicating effective suppression of non-radiative recombination due to the coordination between DCC and Pb dangling bonds at the $CsPbBr_3$ interface. However, when the DCC concentration reaches 30 mg $mL^{-1}$, the PL intensity decreases slightly, likely because the presence of excessive DCC, an insulating material, hinders efficient exciton recombination. The highest PL intensity is achieved at a concentration of 20 mg $mL^{-1}$.

A clearly negative electrostatic potential picture is presented in Fig. 2(e), which is observed around the nitrogen atoms (red region), attributed to the presence of lone-pair electrons. In the carbodiimide (N=C=N) backbone, each nitrogen atom adopts $sp^2$ hybridization: two hybrid orbitals form σ bonds with carbon, the third accommodates a lone pair, and one p orbital participates in π-bonding. The presence of these nitrogen lone-pair electrons results in both the coordination between DCC and Pb dangling bonds and the formation of the dipole, consistent with the observations in Fig. 2(c). The DCC molecules show dual interactions. Firstly, DCC upshifts the energy level of $CsPbBr_3$ *via* the dipole effect. Moreover, it also reduces non-radiative recombination *via* the coordination of DCC and Pb dangling bonds. Fig. 2(f) shows how the dipole effect influences the interfacial energy levels.

As shown in Table 1, the $V_{OC}$ increases with the DCC concentration up to 20 mg $mL^{-1}$, and then declines. This result is attributed to the elevated $CsPbBr_3$ Fermi level, which increases the interface barrier to facilitate the hole transport. The performance degradation at 30 mg $mL^{-1}$ stems from the increased defect density caused by excessive DCC. $J_{sc}$ and FF show no significant changes after the introduction of DCC, except for a slight decrease at 30 mg $mL^{-1}$ due to the hindered exciton recombination by the excessive insulating DCC.

### 2.2 Influence of $NH_4F$ at the $SnO_2$/$CsPbBr_3$ interface

When $NH_4F$ is used to modify the $SnO_2$ interface, F atoms are incorporated into the $SnO_2$ lattice. Owing to the similar ionic radii of F and O, F undergoes a substitutional doping process by occupying O sites. In this study, first-principles simulations of F doping were performed at concentrations of 0%, 0.93%, 4.17%, and 12.5% (the model was constructed as shown in Fig. S5). The relevant calculation parameters and results are provided in Fig. S6–S9 and Table S1. This work mainly focuses on the effects of F doping on the electronic structure of $SnO_2$ at concentrations of 0%, 0.93%, and 4.17%.

As shown in Fig. 3(a–c), as the F doping concentration is increased, the Fermi level of $SnO_2$ gradually shifts from the valence band maximum (Fig. 3(a)) toward the conduction band minimum (Fig. 3(c)), indicating an increase in electron concentration. The upward shift of the Fermi level relative to the valence band maximum reflects a transition from semiconducting to metallic behavior.

As shown in Fig. 3(d–f), the occupied state density of Sn near the Fermi level increases with increasing F doping concentration, primarily contributed by Sn 5s orbitals along with a minor contribution from Sn 5p orbitals.

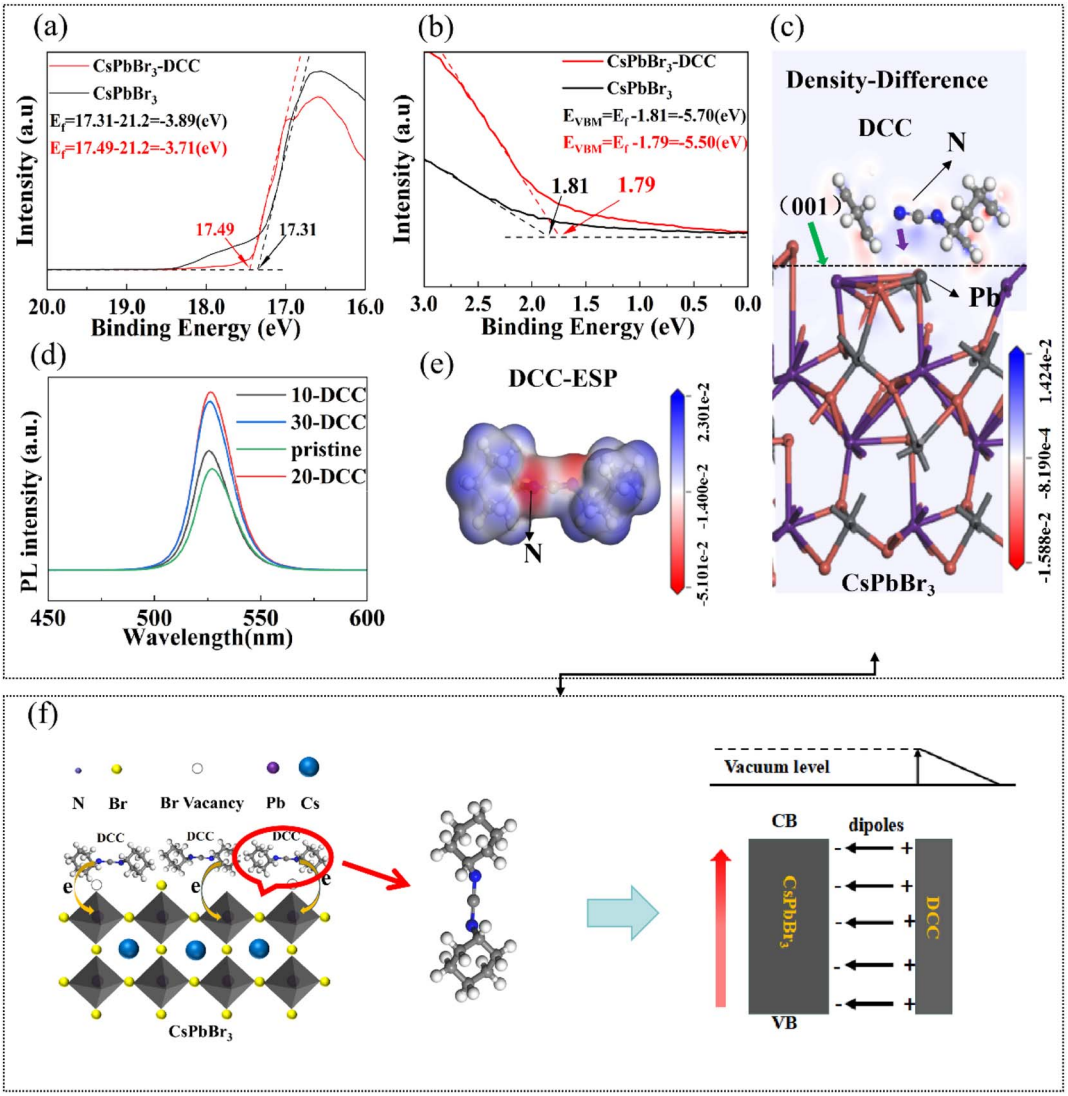


Fig. 2 (a) Cutoff energy of DCC-modified and unmodified $CsPbBr_3$. (b) Onset binding energy of DCC-modified and unmodified $CsPbBr_3$. (c) Differential charge density of a DCC molecule adsorbed on the $CsPbBr_3$ surface. (d) Photoluminescence (PL) spectra of $CsPbBr_3$ with different concentrations of DCC molecules. (e) Electrostatic potential distribution of DCC molecules simulated using first-principles calculations. (f) Adsorption configuration and schematic diagram of the energy level changes induced by DCC modification. Note: DCC solutions (10, 20, and 30 mg $mL^{-1}$ in dichloromethane) are labeled as 10-DCC, 20-DCC, and 30-DCC. $V_{OC}$, $J_{sc}$, FF, and PCE denote open-circuit voltage, short-circuit current density, fill factor, and power conversion efficiency, respectively.

Table 1 Photovoltaic parameters of pristine and DCC-modified $CsPbBr_3$ PSCs

| Device | $J_{sc}$ (mA $cm^{-2}$) | $V_{OC}$ (V) | FF (%) | PCE (%) |
|---|---|---|---|---|
| Pristine | 7.54 | 1.37 | 68.9 | 7.11 |
| 10-DCC | 7.55 | 1.45 | 70.1 | 7.57 |
| 20-DCC | 7.58 | 1.53 | 71.5 | 8.29 |
| 30-DCC | 7.57 | 1.51 | 70.3 | 8.03 |

The distribution of O states remains largely unchanged with increasing F doping concentration (Fig. 4(a–c)), while the F states are predominantly located around −10 eV, with no notable density at the Fermi level (Fig. 4(d–f)). These results indicate that neither O nor F contributes directly to the DOS near the Fermi level; the observed increase in this region is primarily attributed to Sn. Thus, the Fermi level rise is attributed to F substitutional doping at O sites. Owing to its higher electronegativity, F exists as $F^-$, introducing excess electrons that preferentially occupy Sn 5s and 5p orbitals (the primary components of the $SnO_2$ conduction band minimum). Consequently, increased F doping raises the electron concentration in the conduction band, shifting the Fermi level upward. The F 2p states appear around −10 eV (Fig. 4(d–f)), which further confirms $F^-$ formation.

The electrostatic potential distribution of $NH_4F$ (Fig. 5(a)) reveals a negative potential around the F atom, consistent with the strong electronegativity of fluorine. Based on the optimal crystallinity at 0.06 M $L^{-1}$, $SnO_2$ modified with this

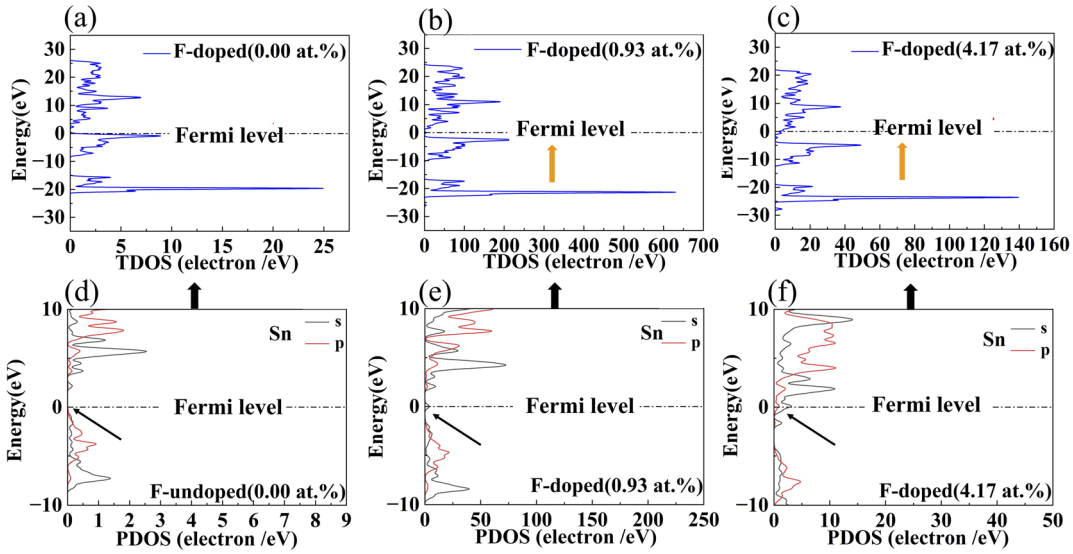


Fig. 3 (a–c) Total DOS of F-doped $SnO_2$. (d–f) Partial DOS of Sn.

concentration was selected for UPS characterization (Fig. 5(b and c)). After $NH_4F$ modification, the secondary electron cutoff increases from 17.15 eV to 17.23 eV, corresponding to a 0.08 eV upward shift of the Fermi level, consistent with the first-principles predictions.

The EIS results (Fig. 5(d)) show that $NH_4F$ modification can increase the arc radius, indicating higher shunt resistance due to the improved $CsPbBr_3$ crystallinity and reduced leakage current. At 0.08 M $L^{-1}$, the arc radius decreases, consistent with pinhole-induced leakage. Thus, $NH_4F$ modification elevates the Fermi level of $SnO_2$ (ref. 28) and improves the crystalline quality of the $CsPbBr_3$ film.

The SEM images (Fig. 5(e–h)) show that the unmodified film exhibits uneven grain distribution (Fig. 5(e)). As the $NH_4F$ concentration increases, the crystallinity improves, reaching a maximum at 0.06 M $L^{-1}$ (Fig. 5(g)). At 0.08 M $L^{-1}$, pinholes appear (Fig. 5(h)), indicating degraded film quality. This behavior is attributed to the $F^-$ ions introduced on the $SnO_2$ surface upon $NH_4F$ treatment. These $F^-$ ions act as Lewis base sites, forming weak coordination with $Pb^{2+}$ and increasing heterogeneous nucleation density during $CsPbBr_3$ crystallization. According to classical nucleation theory, higher nucleation density reduces the critical nucleation radius, promoting denser films with improved grain uniformity. However, excessive $NH_4F$ leads to over-substitution of the surface –OH groups with Sn–F, rendering the $SnO_2$ surface overly hydrophobic and causing dewetting, which results in pinhole formation.

As shown in Table 2, the FF increases with $NH_4F$ concentration up to 0.06 M $L^{-1}$ and then decreases, while $V_{oc}$ and $J_{sc}$ show no significant changes. The FF improvement is attributed to the upshifted $SnO_2$ Fermi level, which optimizes energy level alignment with $CsPbBr_3$ and facilitates electron transport. The decline

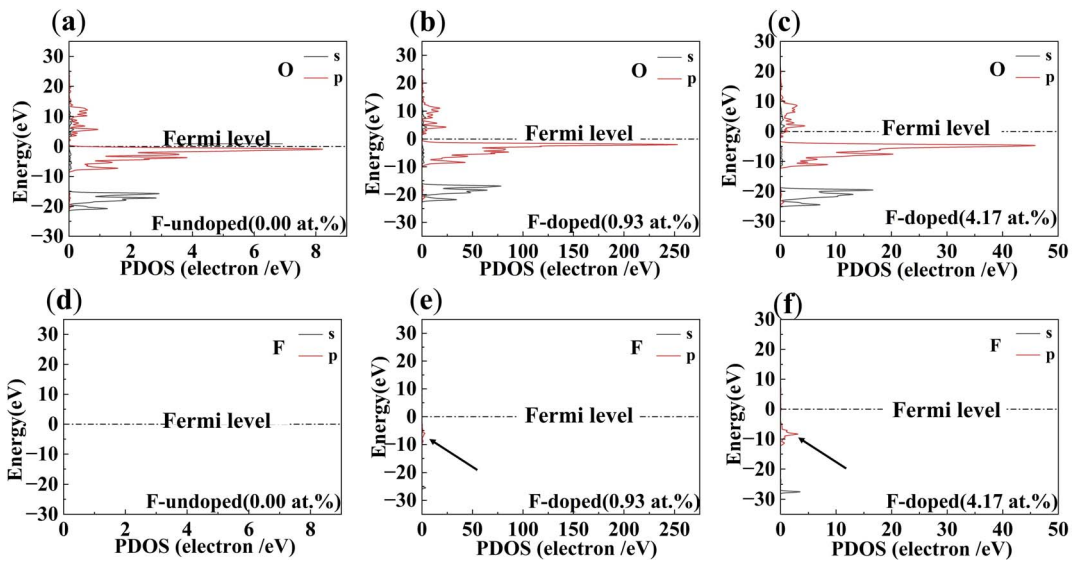


Fig. 4 (a–f) Partial density of states of O and F.

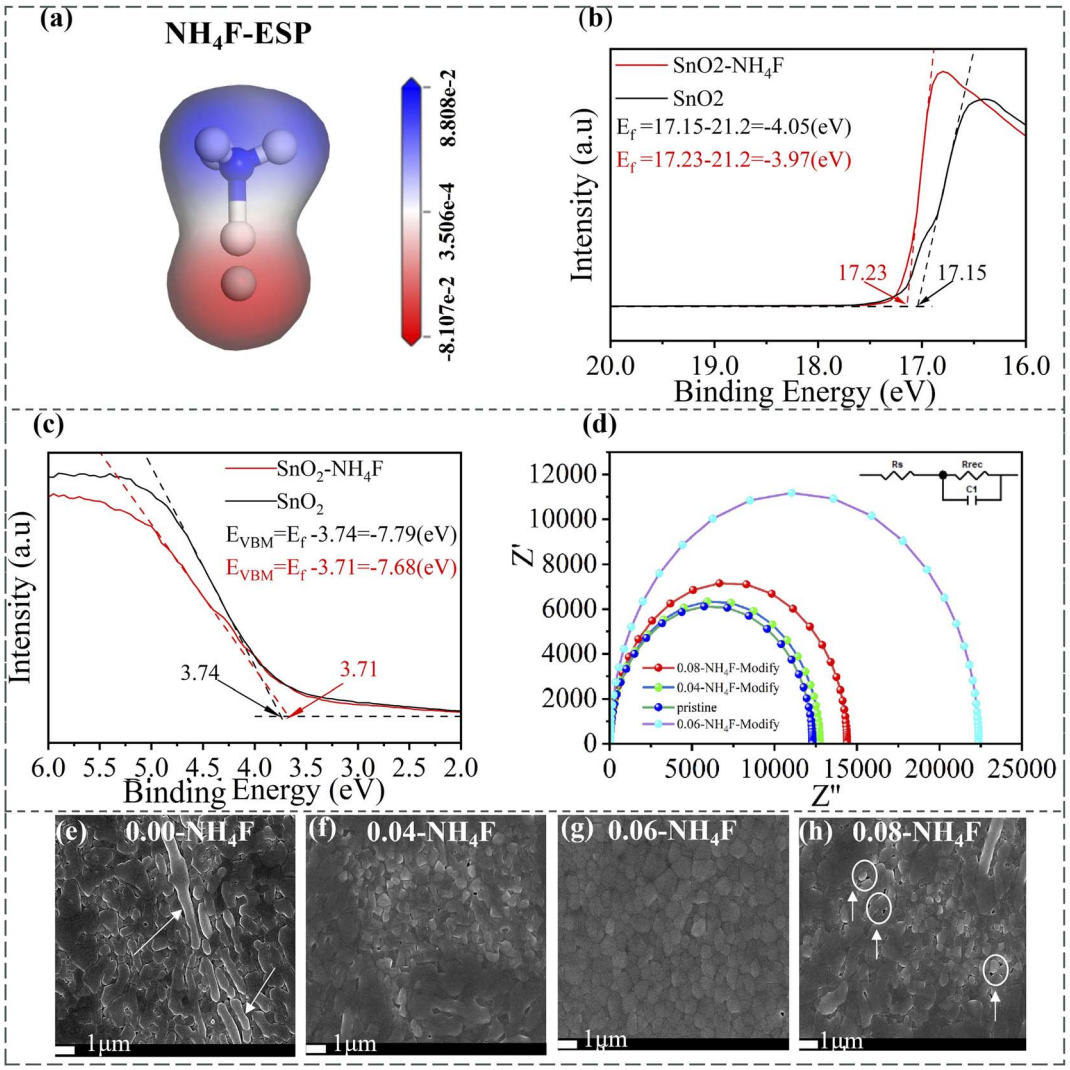


Fig. 5 (a) Electrostatic potential of $NH_4F$ simulated using first-principles calculations. (b and c) UPS characterization of $SnO_2$ before and after $NH_4F$ modification. (d) EIS characterization of the ITO/$SnO_2$/$NH_4F$/$CsPbBr_3$/C device after $NH_4F$ modification. (e–h) SEM images of $CsPbBr_3$ deposited on $SnO_2$ substrates with different $NH_4F$ concentrations.

at higher concentrations is derived from the excessive $NH_4F$ introducing additional non-radiative recombination centers.

### 2.3 Synergistic modification of $CsPbBr_3$ with $NH_4F$ and DCC

Fig. 6(a) shows that the dark current is significantly reduced after the modification, which is attributed to the improved crystalline quality of $CsPbBr_3$, consistent with the results shown in Fig. 5(e) and (g). The device stability is markedly enhanced after synergistic modification (Fig. 6(b)). This is mainly due to the DCC modification layer, which partially suppresses erosion by moisture and oxygen. Fig. 6(c) presents a *J–V* curve closer to ideal diode behavior, with noticeably increased $V_{OC}$ and FF; the corresponding parameters are summarized in Table 3. The underlying physical mechanisms will be discussed in detail in the following section. As shown in Fig. 6(d), the majority of the sample data lie within the boxes, and the number of invalid data points is minimal, satisfying the statistical criteria.

Table 2 Photovoltaic parameters of pristine and $NH_4F$-modified $SnO_2$ PSCs[a]

| Device | $J_{sc}$ (mA cm$^{-2}$) | $V_{OC}$ (V) | FF (%) | PCE (%) |
|---|---|---|---|---|
| Pristine | 7.54 | 1.37 | 68.9 | 7.11 |
| 0.04-$NH_4F$ | 7.56 | 1.37 | 76.0 | 7.87 |
| 0.06-$NH_4F$ | 7.60 | 1.38 | 80.2 | 8.41 |
| 0.08-$NH_4F$ | 7.59 | 1.36 | 78.0 | 8.05 |

[a] $NH_4F$ solutions in deionized water at concentrations of 0.04, 0.06, and 0.08 M are labeled as 0.04-$NH_4F$, 0.06-$NH_4F$, and 0.08-$NH_4F$.

## 3. A simplified explanation

Based on these results, we constructed a theoretical model to elucidate the mechanisms by which the different interfaces influence key device parameters.

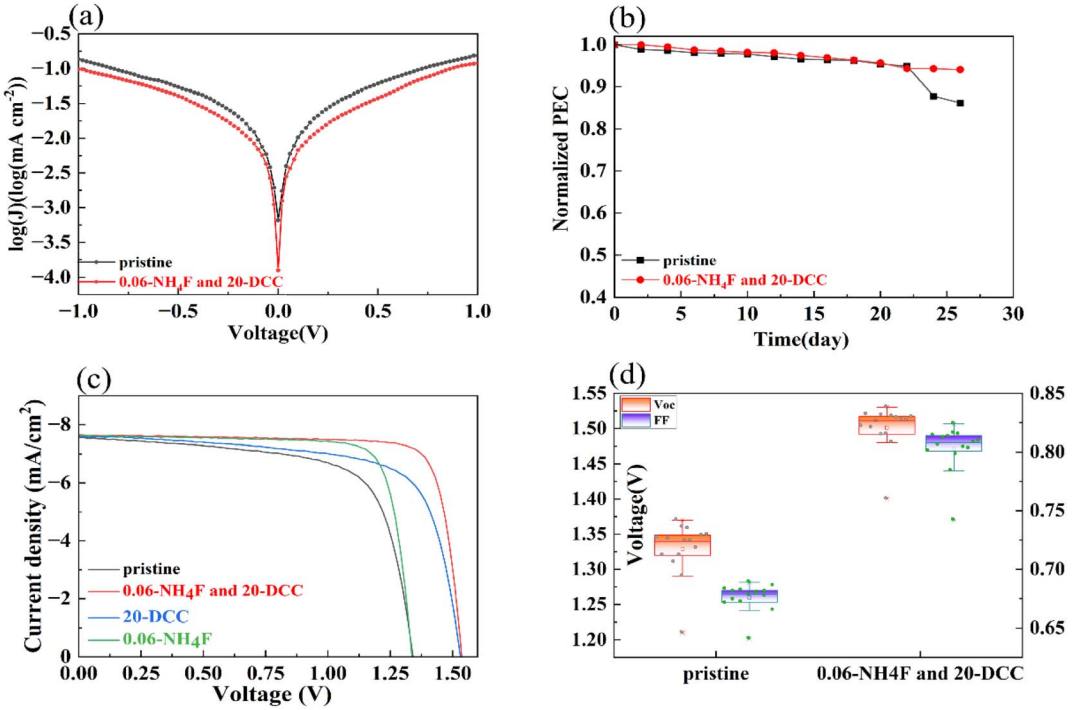


Fig. 6 (a) Dark current measurements of the control device (ITO/$SnO_2$/$CsPbBr_3$/C) and the synergistic interface-modified device (ITO/$SnO_2$/$NH_4F$/$CsPbBr_3$/DCC/C). (b) Stability test results of the corresponding devices. (c) *J*–*V* curves. (d) Statistical comparison of $V_{OC}$ and FF values measured from 15 pristine and 15 synergistically modified samples.

Table 3 Photovoltaic parameters of pristine and $NH_4F$- and DCC-modified $SnO_2$ PSCs

| Device | $J_{sc}$ (mA $cm^{-2}$) | $V_{OC}$ (V) | FF (%) | PCE (%) |
|---|---|---|---|---|
| Pristine | 7.54 | 1.37 | 68.9 | 7.11 |
| 0.06-$NH_4F$/20-DCC | 7.61 | 1.53 | 82.4 | 9.59 |

### 3.1 Establishment of the dual-diode series model (DDSM)

In carbon-based $CsPbBr_3$ PSCs, charge transport interfaces are primarily formed between $CsPbBr_3$ and the carbon electrode, and between $CsPbBr_3$ and the $SnO_2$ electron transport layer (Fig. 7(a)). The $CsPbBr_3$/C interface has a higher barrier than the $SnO_2$/$CsPbBr_3$ interface (Fig. 7(b)). We define the high-barrier $CsPbBr_3$/C interface as diode D1 and the low-barrier $SnO_2$/$CsPbBr_3$ interface as diode D2. As they are both Schottky contacts, the structure can be modeled as a dual-diode series model (DDSM) (Fig. 7(c)). Based on this model, the current–voltage characteristics can be derived. Parameters are defined in Note S3.

$$I_1 = I_{s1}[e^{(qV_1/KT)} - 1] \quad (1)$$

$$I_2 = I_{s2}[1 - e^{(-qV_2/KT)}] \quad (2)$$

$$V = V_1 + V_2 \quad (3)$$

$$I_{s1} \propto e^{\left(\frac{-qV_{D1}}{KT}\right)}, \quad I_{s2} \propto e^{\left(\frac{-qV_{D2}}{KT}\right)} \quad (4)$$

From the equation for series current ($I_1 = I_2$), we can obtain the following (Note S1).

$$I = \frac{I_{s1}I_{s2}\left(1 - e^{\frac{-qV}{KT}}\right)}{I_{s1} + I_{s2}\, e^{\frac{-qV}{KT}}} \quad (5)$$

### 3.2 Relationship between the $CsPbBr_3$/C interface barrier ($eV_{D1}$) and $V_{OC}$

Since $eV_{D1} \gg eV_{D2}$, under an applied voltage $V$, $V_1 \gg V_2$, and $V \approx V_1$. Combining eqn (2) and (5) gives:

$$I = I_1 \approx I_{s1}\left[e^{\left(\frac{qV}{KT}\right)} - 1\right] \quad (6)$$

When $e^{\left(\frac{qV}{kT}\right)} \gg 1$, the *I*–*V* relationship is satisfied.

$$I \approx I_{s1}\, e^{\left(\frac{qV}{KT}\right)} \quad (7)$$

Under open-circuit conditions, the current satisfies $I = I_{sc}$, and $e^{\left(\frac{qV_{OC}}{kT}\right)} \gg 1$ Combining eqn (4) and (7) gives:

$$I_{sc} = C\, e^{\left(\frac{-qV_{D1}}{KT}\right)}\, e^{\left(\frac{qV_{OC}}{KT}\right)} \quad (8)$$

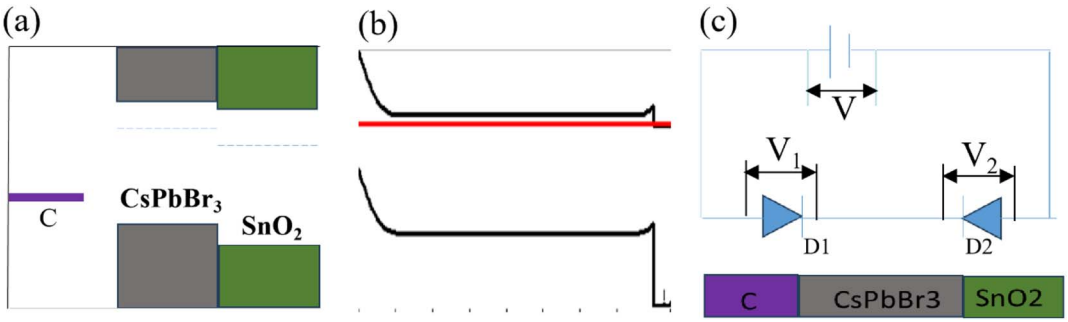


Fig. 7 (a) $SnO_2$/$CsPbBr_3$/C heterojunction. (b) Energy level alignment of $SnO_2$/$CsPbBr_3$/C heterojunction. (c) Dual-diode series model (DDSM).

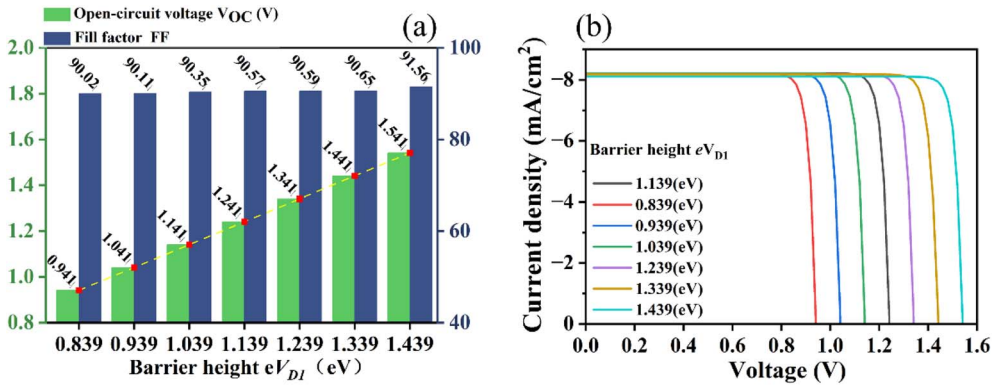


Fig. 8 (a) Variation of the $V_{OC}$ and FF of the device under different $eV_{D1}$ at the CsPbBr$_3$/C interface. (b) $J$–$V$ curves corresponding to different $eV_{D1}$ at the CsPbBr$_3$/C interface.

$$V_{oc} = \frac{KT}{q}\ln\frac{I_{sc}}{C} + V_{D1} \quad (9)$$

Using $V_{D1} = \frac{E_{f(CsPbBr_3)} - E_{f(C)}}{q}$, we obtain:

$$V_{oc} = \frac{KT}{q}\ln\frac{I_{sc}}{C} + \frac{E_{ef(CsPbBr_3)} - E_{ef(C)}}{q} \quad (10)$$

Under a constant $I_{sc}$ and carbon Fermi level, $\Delta V_{oc} = \frac{\Delta V_{D1}}{q} = \frac{\Delta E_{ef(CsPbBr_3)}}{q}$, indicating a linear relationship between $\Delta V_{oc}$ and $\Delta V_{D1}$ (Note S4).

Fig. 8 shows the results of the SCAPS-1D simulation for the $V_{OC}$ and $J$–$V$ curves under varying $eV_{D1}$; relevant details are provided in Table S2. The SCAPS-1D simulations (Fig. 8(a)) confirm a linear relationship: as $eV_{D1}$ increases, $V_{OC}$ increases linearly while the fill factor (FF) remains approximately 90%, indicating that $eV_{D1}$ primarily influences $V_{OC}$ with minimal impact on FF. Fig. 8(b) also shows that the $V_{OC}$ increases linearly with $eV_{D1}$, as indicated by the intersection of the curve with the horizontal axis. These results are consistent with the data in Tables 1, 3, and Fig. 2(a). After DCC modification, the $V_{OC}$ increases from 1.37 V to 1.53 V, corresponding to an increment of 0.16 V. This value closely aligns with the increase of 0.18 eV in

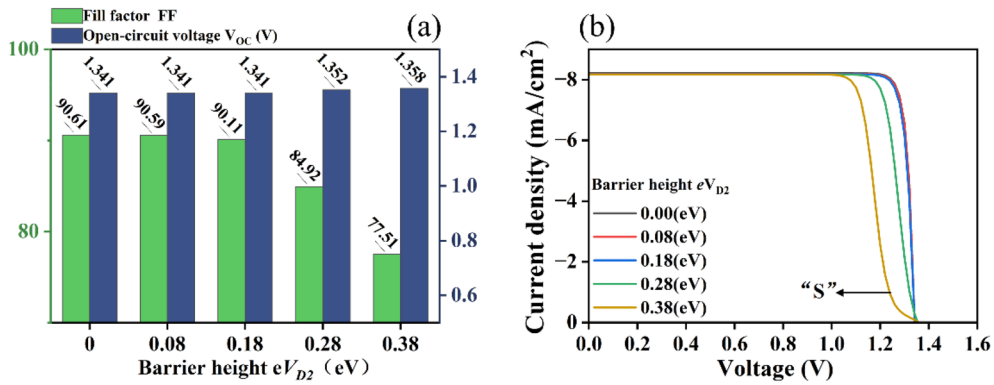


Fig. 9 (a) Variation of the open-circuit voltage and fill factor of the device under different barrier heights $eV_{D2}$ at the $SnO_2$/$CsPbBr_3$ interface. (b) $J$–$V$ curves corresponding to different barrier heights $eV_{D2}$ at the $SnO_2$/$CsPbBr_3$ interface.

the Fermi level. The slight discrepancy of 0.02 V is mainly attributed to non-radiative recombination. Therefore, the experimental results are in strong agreement with the model conclusions.

### 3.3 Relationship between the $SnO_2$/$CsPbBr_3$ interface barrier ($eV_{D2}$) and FF

In the actual system, the $SnO_2$/$CsPbBr_3$ interface can induce a voltage $V_2$, causing deviation from ideal diode behavior *via* eqn (5). This deviation is a key factor in FF reduction. When the $SnO_2$ Fermi level is shifted relative to $CsPbBr_3$, $eV_{D2}$ is decreased, and $I_{s2}$ is increased (eqn (4)). In this series configuration, $V_1$ increases while $V_2$ decreases, increasing the FF (Note S5). At large $eV_{D2}$ values, $I_{s2}$ becomes extremely small, leading to an S-shaped *J–V* distortion and a sharp FF drop.

SCAPS-1D simulations (Fig. 9) showed that as $eV_{D2}$ increases from 0 eV to 0.38 eV, the FF first decreases gradually and then drops sharply beyond a threshold of 0.28 eV, while the $V_{OC}$ remains relatively stable. As shown in Fig. 9(b), when $eV_{D2}$ reaches 0.38 eV, the *J–V* curve exhibits a pronounced S-shaped distortion (orange curve). These results indicate that $eV_{D2}$ primarily governs the FF, with a negligible influence on the $V_{OC}$. Combined with the data in Fig. 5(b), Tables 2 and 3, after modifying $SnO_2$ with $NH_4F$, the Fermi level increases by 0.08 eV, and the fill factor improves from 68.9% to 82.4%. This trend is consistent with the model and simulation results.

## 4. Conclusion

We demonstrated a synergistic dual-interface modification strategy that decouples the enhancement of $V_{OC}$ and FF in $CsPbBr_3$ PSCs by independently targeting the $CsPbBr_3$/carbon and $SnO_2$/$CsPbBr_3$ interfaces. More importantly, we established a dual-diode series model (DDSM) that quantitatively correlates $V_{OC}$ with the $CsPbBr_3$/C barrier in a linear manner. These results revealed that a larger barrier at the $SnO_2$/$CsPbBr_3$ interface would lead to more pronounced degradation of the FF. The excellent agreement among the theoretical model, SCAPS-1D simulations, and experimental results validated the DDSM as a powerful analytical tool for decoupling interfacial contributions. This work will provide a rational framework for interface design in all-inorganic PSCs and could be extended to other wide-bandgap perovskite systems facing similar interfacial challenges.

## Conflicts of interest

The authors have declared that no conflicting interests exist.

## Data availability

The data that support the findings of this study are available within the paper and its supplementary information (SI). The raw experimental data (including *J–V* curves, UPS, PL, SEM, EIS) and the simulation input/output files (first-principles DFT and SCAPS-1D) are available from the corresponding authors upon reasonable request. Supplementary information is available. See DOI: https://doi.org/10.1039/d6ra02943d.

## Acknowledgements

These works were supported by Guizhou Province High level Talent Training Plan (100 Levels) (No. QKHPTRC-GCC[2023] 089); Guizhou Province Natural Science Foundation (Qiankehe Fundamentals – ZK[2024]General-106).

## References

1 T. Nie, L. Jia, J. Feng, S. Yang, J. Ding, S. Liu and Z. Fang, Advances in Single-Halogen Wide-Bandgap Perovskite Solar Cells, *Adv. Funct. Mater.*, 2025, **35**(9), 2416264, DOI: 10.1002/adfm.202416264.

2 D. A. Egger, A. M. Rappe and L. Kronik, Hybrid Organic–Inorganic Perovskites on the Move, *Acc. Chem. Res.*, 2016, **49**, 573–581, DOI: 10.1021/acs.accounts.5b00540.

3 T. Umebayashi, K. Asai, T. Kondo and A. Nakao, Electronic structures of lead iodide based low-dimensional crystals, *Phys. Rev. B: Condens. Matter Mater. Phys.*, 2003, **67**, 155405, DOI: 10.1103/PhysRevB.67.155405.

4 J. Duan, M. Wang, Y. Wang, J. Zhang, Q. Guo, Q. Zhang, Y. Duan and Q. Tang, Effect of Side-Group-Regulated Dipolar Passivating Molecules on CsPbBr3 Perovskite Solar Cells, *ACS Energy Lett.*, 2021, **6**, 2336–2342, DOI: 10.1021/acsenergylett.1c01060.

5 E. L. Unger, L. Kegelmann, K. Suchan, D. Sörell, L. Korte and S. Albrecht, Roadmap and roadblocks for the band gap tunability of metal halide perovskites, *J. Mater. Chem. A*, 2017, **5**, 11401–11409, DOI: 10.1039/c7ta00404d.

6 F. Peña-Camargo, P. Caprioglio, F. Zu, E. Gutierrez-Partida, C. M. Wolff, K. Brinkmann, S. Albrecht, T. Riedl, N. Koch, D. Neher and M. Stolterfoht, Halide Segregation versus Interfacial Recombination in Bromide-Rich Wide-Gap Perovskite Solar Cells, *ACS Energy Lett.*, 2020, **5**, 2728–2736, DOI: 10.1021/acsenergylett.0c01104.

7 P. Caprioglio, C. M. Wolff, O. J. Sandberg, A. Armin, B. Rech, S. Albrecht, D. Neher and M. Stolterfoht, On the Origin of the Ideality Factor in Perovskite Solar Cells, *Adv. Energy Mater.*, 2020, **10**(27), 2000502, DOI: 10.1002/aenm.202000502.

8 B.-Y. Liu, H.-M. Yang, Y.-D. Zuo, Z.-H. Tao, J.-C. Li, Y.-J. Chang, G.-Q. Tong and Y. Jiang, Intermediate phase-assisted growth of CsPbBr3 for high performance of carbon-based perovskite solar cells, *Rare Met.*, 2024, **43**, 2222–2229, DOI: 10.1007/s12598-023-02578-5.

9 C. Liu, T. Zhang, Z. Li, B. Zhao, X. Ma, Y. Chen, Z. Liu, H. Chen and X. Li, Crystallization Kinetics Engineering toward High-Performance and Stable CsPbBr3-Based Perovskite Solar Cells, *ACS Appl. Energy Mater.*, 2021, **4**, 10610–10617, DOI: 10.1021/acsaem.1c01593.

10 D. Wang, W. Li, Z. Du, G. Li, W. Sun, J. Wu and Z. Lan, Highly Efficient CsPbBr3 Planar Perovskite Solar Cells via Additive Engineering with NH4SCN, *ACS Appl. Mater. Interfaces*, 2020, **12**, 10579–10587, DOI: 10.1021/acsami.9b23384.

11 W. Shao, J. Sheng, Y. Fu, J. He, Z. Deng, R. Cen and W. Wu, Achieving unprecedented power-output in 4-terminal mirror-symmetrical printable carbon CsPbBr3 solar cells through dual-solvent engineering, *Energy Environ. Sci.*, 2025, **18**, 3211–3222, DOI: 10.1039/d4ee05841k.

12 J. Bi, J. Chang, M. Lei, W. Zhang, F. Meng and G. Wang, Thiourea-Assisted Facile Fabrication of High-Quality CsPbBr3 Perovskite Films for High-Performance Solar Cells, *ACS Appl. Mater. Interfaces*, 2022, **14**, 48888–48896, DOI: 10.1021/acsami.2c13658.

13 W. Zhang, X. Liu, B. He, Z. Gong, J. Zhu, Y. Ding, H. Chen and Q. Tang, Interface Engineering of Imidazolium Ionic Liquids toward Efficient and Stable CsPbBr3 Perovskite Solar Cells, *ACS Appl. Mater. Interfaces*, 2020, **12**, 4540–4548, DOI: 10.1021/acsami.9b20831.

14 Q. Zhou, J. Duan, J. Du, Q. Guo, Q. Zhang, X. Yang, Y. Duan and Q. Tang, Tailored Lattice "Tape" to Confine Tensile Interface for 11.08%-Efficiency All-Inorganic CsPbBr3 Perovskite Solar Cell with an Ultrahigh Voltage of 1.702 V, *Adv. Sci.*, 2021, **8**(19), 2101418, DOI: 10.1002/advs.202101418.

15 L. Zhou, M. Sui, J. Zhang, K. Cao, H. Wang, H. Yuan, Z. Lin, J. Zhang, P. Li, Y. Hao and J. Chang, Tailored buried layer passivation toward high-efficiency carbon based all-inorganic CsPbBr3 perovskite solar cell, *Chem. Eng. J.*, 2024, **496**, 154043, DOI: 10.1016/j.cej.2024.154043.

16 S. Mohammadi and S. Akbari Nia, Optimizing the perovskite/SnO2 interface: Defect passivation and energy level alignment for high-efficiency perovskite solar cells, *J. Power Sources*, 2025, **655**, 237926, DOI: 10.1016/j.jpowsour.2025.237926.

17 C. Ding, Y. Zhang, F. Liu, Y. Kitabatake, S. Hayase, T. Toyoda, K. Yoshino, T. Minemoto, K. Katayama and Q. Shen, Effect of the conduction band offset on interfacial recombination behavior of the planar perovskite solar cells, *Nano Energy*, 2018, **53**, 17–26, DOI: 10.1016/j.nanoen.2018.08.031.

18 Y. Zhao, B. Pang, S. Zheng, X. Kong, M. Zhao, H. Dong, L. Yu and L. Dong, Enhanced Performance and Stability of CsPbBr3 Perovskite Solar Cells Using Trioctylphosphine Oxide Additive, *ACS Appl. Mater. Interfaces*, 2024, **16**, 69410–69417, DOI: 10.1021/acsami.4c15862.

19 X. Jiang, C. Geng, X. Yu, J. Pan, H. Zheng, C. Liang, B. Li, F. Long, L. Han, Y.-B. Cheng and Y. Peng, Doping with KBr to Achieve High-Performance CsPbBr3 Semitransparent Perovskite Solar Cells, *ACS Appl. Mater. Interfaces*, 2024, **16**, 19039–19047, DOI: 10.1021/acsami.4c02402.

20 S. Tang, M. Liao, W. Sun, J. Wu, J. Lu and Y. Xie, Optimizing CsPbBr3 perovskite solar cell interface and performance through tetraphenylethene derivatives, *Chin. Chem. Lett.*, 2025, **36**(06), 110838, DOI: 10.1016/j.cclet.2025.110838.

21 A. Tong, X. Chen, Y. Wang, Y. Wang, Q. Zheng, R. He, Z. Jin, W. Sun, Y. Li and J. Wu, Energy Level Tuning in CsPbBr3 Perovskite Solar Cells through In Situ-Polymerized PEDOT Hole Transport Layer, *ACS Appl. Mater. Interfaces*, 2024, **16**, 50640–50649, DOI: 10.1021/acsami.4c08526.

22 S. Gao, X. Li, R. Cao, X. Li, T. Chen, Y. Lu, J. Zhu and S. Yang, Hot Pure Oxygen Accelerated Oxidation of Spiro-OMeTAD for Efficient Perovskite Solar Cells with a Record Certified Fill Factor Exceeding 87%, *ACS Energy Lett.*, 2024, **9**, 5037–5044, DOI: 10.1021/acsenergylett.4c01912.

23 A. Razzaq, A. Ullah, A. S. Subbiah and S. De Wolf, Practical Fill Factor Limits for Perovskite Solar Cells, *ACS Energy Lett.*, 2024, **9**, 5635–5638, DOI: 10.1021/acsenergylett.4c02757.

24 Y. Wang, S. Akel, B. Klingebiel and T. Kirchartz, Hole Transporting Bilayers for Efficient Micrometer-Thick Perovskite Solar Cells, *Adv. Energy Mater.*, 2023, **14**(04), 2302614, DOI: 10.1002/aenm.202302614.

25 L. V. Torres Merino, C. E. Petoukhoff, O. Matiash, A. S. Subbiah, C. V. Franco, P. Dally, B. Vishal, S. Kosar, D. Rosas Villalva, V. Hnapovskyi, E. Ugur, S. Shah, F. Peña Camargo, O. Karalis, H. Hempel, I. Levine, R. R. Pradhan, S. Kralj, N. Kalasariya, M. Babics, B. K. Yildirim, A. A. Said, E. Aydin, H. Bristow, S. Mannar, W. Raja, A. R. Pininti, A. Prasetio, A. Razzaq, H. Al Nasser, T. G. Allen, F. H. Isikgor, D. Baran, T. D. Anthopoulos, M. M. Masis, U. Schwingenschlögl, T. Unold, M. Stolterfoht, F. Laquai and S. De Wolf, Impact of the valence band energy alignment at the hole-collecting interface on the photostability of wide band-gap perovskite solar cells, *Joule*, 2024, **8**, 2585–2606, DOI: 10.1016/j.joule.2024.06.017.

26 Y.-J. Huang, C.-E. Cai, Y.-C. Feng, B.-T. Liu and R.-H. Lee, Water-Soluble Cationic Copolyacrylamides Modifying NiOx for High-Performance Inverted Perovskite Solar Cells, *ACS Appl. Polym. Mater.*, 2023, **5**, 8949–8959, DOI: 10.1021/acsapm.3c01396.

27 J. Zhu, Y. Liu, B. He, W. Zhang, L. Cui, S. Wang, H. Chen, Y. Duan and Q. Tang, Efficient interface engineering of N, N'-Dicyclohexylcarbodiimide for stable HTMs-free CsPbBr3 perovskite solar cells with 10.16%-efficiency, *Chem. Eng. J.*, 2022, **428**, 131950, DOI: 10.1016/j.cej.2021.131950.

28 E. H. Jung, B. Chen, K. Bertens, M. Vafaie, S. Teale, A. Proppe, Y. Hou, T. Zhu, C. Zheng and E. H. Sargent, Bifunctional Surface Engineering on SnO2 Reduces Energy Loss in Perovskite Solar Cells, *ACS Energy Lett.*, 2020, **5**, 2796–2801, DOI: 10.1021/acsenergylett.0c01566.